

LETTER TO THE EDITOR

Dust/gas correlations from Herschel observations[★]

J. Roman-Duval¹, F.P. Israel², A. Bolatto³, A. Hughes^{4,5}, A. Leroy⁶, M. Meixner¹, K. Gordon¹, S.C. Madden⁷, D. Paradis⁸, A. Kawamura⁹, A. Li¹⁰, M. Sauvage⁷, T. Wong¹¹, J.-P. Bernard¹², C. Engelbracht¹³, S. Hony⁷, S. Kim¹⁴, K. Misselt¹³, K. Okumura⁷, J. Ott¹⁵, P. Panuzzo⁷, J.L. Pineda¹⁶, W.T. Reach^{8,17}, M. Rubio¹⁸

(Affiliations can be found after the references)

Received March 30, 2010; accepted ..., 2010

ABSTRACT

Context. Previous Spitzer and IRAS observations of the LMC suggest an excess of FIR emission with respect to the gas surface density traced by ¹²CO rotational emission lines and H I 21 cm emission. This so-called “FIR excess” is especially noticeable near molecular clouds in the LMC, and has usually been interpreted as indicating the presence of a self-shielded H₂ component not traced by CO in the envelopes of molecular clouds. **Aims.** Based on Herschel HERITAGE observations taken as part of the Science Demonstration Phase, we examine the correlation between gas and dust surface densities at higher resolution than previously achieved. We consider three additional possible causes for the FIR excess: X factor, FIR dust emissivity, and gas-to-dust ratio variations between the diffuse and dense phases of the ISM.

Methods. We examine the structure of NT80 and NT71, two molecular clouds detected in the NANTEN ¹²CO survey of the LMC. Dust surface density maps were derived from the HERITAGE data. The gas phase is traced by MAGMA ¹²CO and ATCA+Parkes H I 21 cm observations of the LMC. These data provide unprecedented resolution (1′) to examine the structure of molecular clouds. The dust emissivity, gas-to-dust ratio, and X factor required to match the dust and gas surface densities are derived, and their correlations with the dust surface density are examined.

Results. We show that the dust surface density is spatially correlated with the atomic and molecular gas phases. The dust temperature is consistently lower in the dense phase of the ISM than in the diffuse phase. We confirm variations in the ratio of FIR emission to gas surface density derived from H I and CO observations. There is an excess of FIR emission, spatially correlated with regions of intermediate H I and dust surface densities ($A_V = 1-2$), and little or no CO. While there is no significant trend in the dust emissivity or gas-to-dust ratio with dust surface density, the X factor is enhanced at $A_V = 1-2$. We conclude that H₂ envelopes not traced by CO and X factor variations close to the CO boundary may be more likely to cause these deviations between FIR emission and gas surface density than gas-to-dust ratio or emissivity variations.

Key words. ISM: dust, extinction – ISM: clouds – ISM: abundances – ISM: structure – Galaxies: ISM – Galaxies: Magellanic Clouds

1. Introduction

Dust, neutral atomic hydrogen (H I), and molecular hydrogen (H₂) are the prime constituents of the interstellar medium in galaxies out of which stars form, but their amounts are often poorly known. In dense clouds, dust shields both H₂ and its tracer CO from dissociation by the ambient interstellar radiation field (ISRF). Unlike CO, H₂ is also strongly self-shielding. In the solar neighborhood, H₂ forms at $A_V \geq 0.14$, while CO requires $A_V \geq 0.8$ (Wolfire et al. 2010). Molecular clouds (MCs) thus consist of dense cores where CO and H₂ coexist and less dense envelopes of H₂ with little or no CO. In lower-metallicity environments with strong irradiation, the poorly shielded CO fills a much smaller fraction of the H₂ volume. In those galaxies use of a standard conversion factor X_{CO} to estimate H₂ column densities from observed CO emission causes large amounts of H₂ to be missed (see e.g., Glover & Mac Low 2010).

The nearest low-metallicity galaxies are the Large Magellanic Cloud (LMC) and the Small Magellanic Cloud (SMC) with [C] and [O] abundances 0.25/0.50 and 0.10/0.25 relative to solar abundances (Pagel 2003) and distances of 50 kpc (Schaefer 2008) and 62 kpc (Szewczyk et al. 2009) respectively. The FIR emission from dust has been used to establish that indeed much H₂ is not traced by CO and exhibits a so-called

“FIR excess”, implying X factors 3-6 (LMC) and 20-60 (SMC) times higher than in the solar neighborhood (Israel 1997; Leroy et al. 2007, 2009; Bernard et al. 2008). Their analysis assumes that dust grain emissivity and gas-to-dust ratios are the same in dense H₂ clouds and more tenuous H I regions. Our goal in this Letter is to explore whether these assumptions are justified. To this end, we examine the structure of two MCs in the LMC, NT80 and NT71 (Fukui et al. 2008). Both clouds are relatively quiescent (Kawamura et al. 2009), with star formation rates implied by H α and 24 μ m emission of 0.018 and 0.042 M_⊙/kpc²/yr. NT80 is located in a direction practically devoid of H α emission, while NT71 is associated with the faint filamentary H α nebula DEM 110 (Davies et al. 1976). We examine the correlation between dust and gas based on *HERschel Inventory of The Agents of Galactic Evolution* (HERITAGE) data and MAGellanic Mopra Assessment (MAGMA, PI. T. Wong) ¹²CO data. These data provide unprecedented resolution (15 pc) to observe the structure of MCs in the LMC.

2. Observations and dust and gas surface densities

The dust surface density (Σ_{dust}) and temperature T_{dust} in the LMC have been derived in Gordon et al. (2010), based on *Spitzer* MIPS 160 μ m observations from the *Surveying the Agents of Galactic Evolution* project (SAGE, Meixner et al. 2006), and more recent SPIRE (Griffin et al. 2010) observations taken by *Herschel* as part of the HERITAGE key project during the

[★] Herschel is an ESA space observatory with science instruments provided by European-led Principal Investigator consortia and with important participation from NASA.

Science Demonstration Phase (Meixner et al. 2010). The dust temperature was obtained by fitting a modified black body of emissivity law $\beta = 1.5$ to the MIPS 160 μm , SPIRE 250 and 350 μm bands (the 500 μm band being affected by an excess of unknown origin). The dust surface density was derived from the MIPS 160 μm brightness and the dust temperature, assuming that the grains are silicates of density 3 g cm^{-3} , size $a = 0.1 \mu\text{m}$, and emissivity at 160 μm $\epsilon_{160}^0 = 1.7 \times 10^{-17} \text{ m}^2$ (absorption efficiency $Q_{160} = 5.47 \times 10^{-4}$). Figures 1 and 2 show the dust surface density and temperature for NT80 and NT71.

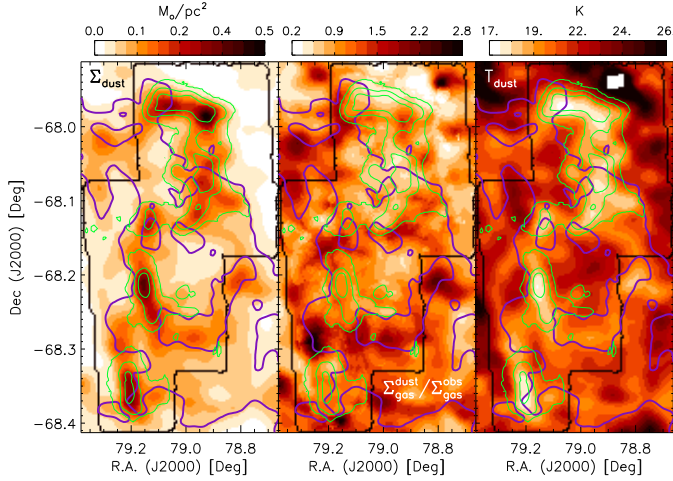


Fig. 1. Dust surface density (left), ratio of the gas surface density implied from dust measurements, $\Sigma_{\text{gas}}^{\text{dust}}$, to the gas surface density derived from H I and CO observations, $\Sigma_{\text{gas}}^{\text{obs}}$ (middle), and dust temperature (right) for NT80. The 3σ level in dust surface density is $0.04 \text{ M}_{\odot}/\text{pc}^2$. The purple contours show the 20, 30, and $40 \text{ M}_{\odot}/\text{pc}^2$ H I surface density. The green contours show the 10, 40, and $80 \text{ M}_{\odot}/\text{pc}^2$ H₂ surface density inferred from CO. The solid black lines show the MAGMA coverage.

The H I column density was taken from the Australian telescope compact array (ATCA)+Parkes map of the LMC by Kim et al. (2003), and converted into a surface density via $\Sigma(\text{H I}) = 1.08 \times 10^{-20} \text{ N}(\text{H I})$, where $\Sigma(\text{H I})$ is the H I surface density in $\text{M}_{\odot}/\text{pc}^2$, and the conversion includes the contribution of He to the mean molecular weight (1.36). We applied the same background subtraction to the dust and H I surface density maps to set the zero level of the sky background at the end points of the HERITAGE scans, located outside of the LMC (Meixner et al. 2010). The molecular gas surface density was derived from MAGMA CO observations via $\Sigma(\text{H}_2^{\text{CO}}) = 2.16 \times 10^{-20} X_{\text{CO}} I_{\text{CO}}$, where $\Sigma(\text{H}_2^{\text{CO}})$ is the molecular gas surface density in $\text{M}_{\odot}/\text{pc}^2$, I_{CO} is the CO integrated intensity in K km/s, and X_{CO} is the X factor. We assume X_{CO} values derived from a virial analysis of NT80 and NT71 by Hughes et al. (2010): $X_{\text{CO}} = (5.1 \pm 0.1) \times 10^{20} \text{ cm}^{-2} \text{ K}^{-1} \text{ km}^{-1} \text{ s}$ for NT80 and $(4.1 \pm 0.1) \times 10^{20} \text{ cm}^{-2} \text{ K}^{-1} \text{ km}^{-1} \text{ s}$ for NT71, consistent with the range of values from Israel (1997) for MCs similar to NT80 and NT71. The implied gas surface density is $\Sigma_{\text{gas}}^{\text{obs}} = \Sigma(\text{H I}) + \Sigma(\text{H}_2^{\text{CO}})$. The sensitivities of the H I and MAGMA maps are 0.9 and $5.5 \text{ M}_{\odot}/\text{pc}^2$ (0.5 K km/s). Atomic and molecular gas surface densities are shown in Figs. 1 and 2.

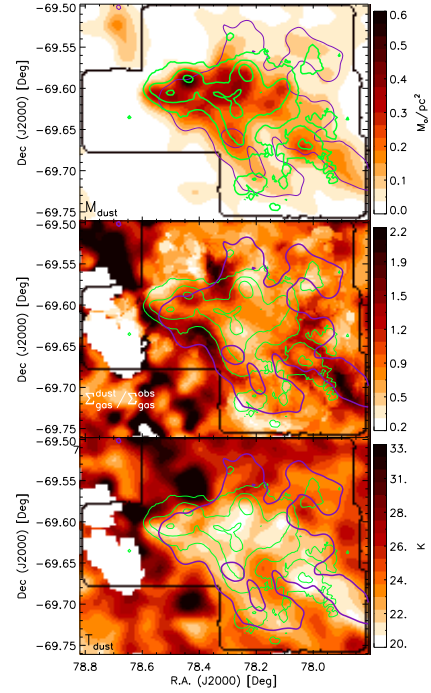


Fig. 2. Same as Fig. 1 for NT71, except that the purple contours represent the 15, 25, and $35 \text{ M}_{\odot}/\text{pc}^2$ levels of H I surface density.

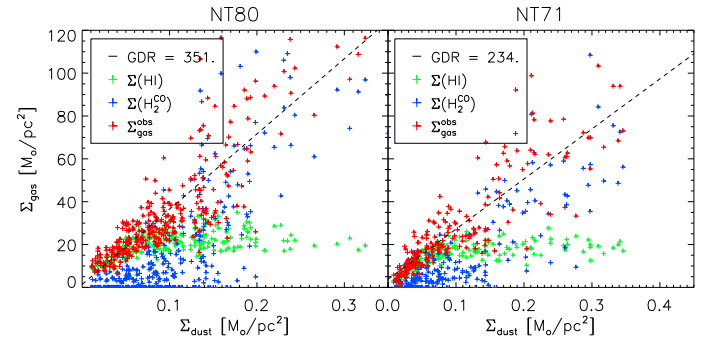


Fig. 3. Gas surface densities of the atomic and molecular phases vs dust surface density. The dashed line represents the gas-to-dust ratio.

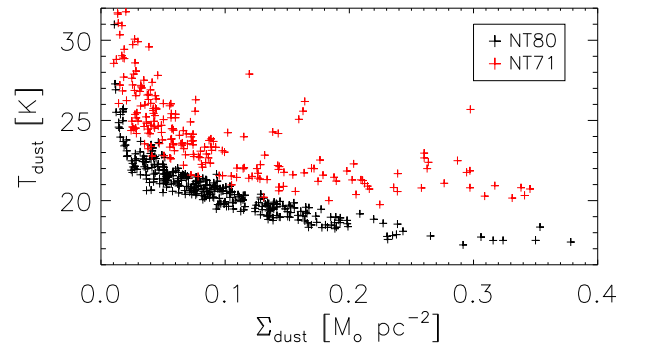


Fig. 4. Correlation between dust surface density and temperature for NT80 (black) and NT71 (red).

3. Dust/gas correlation and FIR excess

The first panels of Figs. 1 and 2 show that the molecular phase traced by CO is very well correlated with the highest dust surface density regions. The $\Sigma_{\text{dust}} > 0.08 \text{ M}_{\odot}/\text{pc}^2$ ($A_V > 0.8$) contour is indeed almost identical to the $5.5 \text{ M}_{\odot}/\text{pc}^2$ contour of $\Sigma(\text{H}_2^{\text{CO}})$

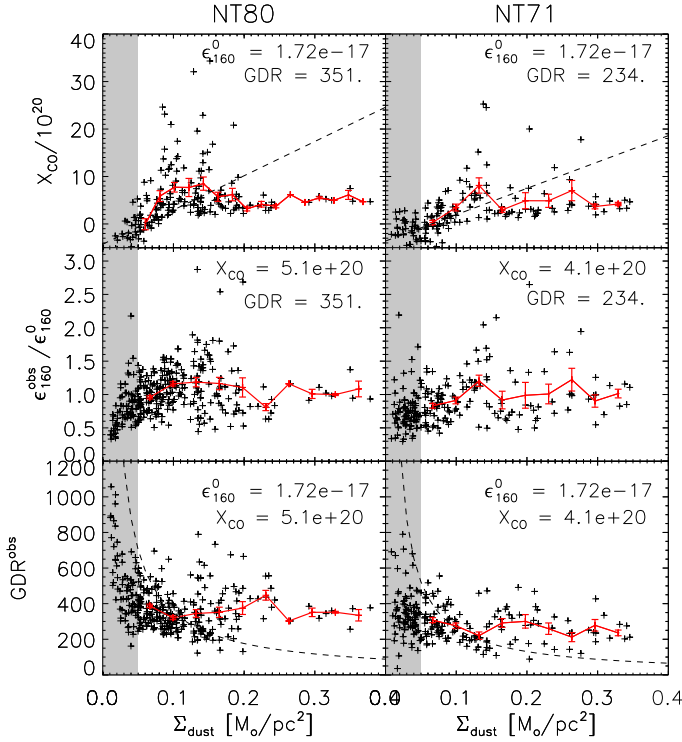


Fig. 5. Correlations between the dust surface density and i) the X factor (top), dust emissivity (middle), and gas-to-dust ratio (bottom) in NT80 (left), and NT71 (right). The dashed lines were obtained from the mean gas surface density, the red curves from the binned trends. Error bars show uncertainty in the mean. The shaded areas correspond to $\Sigma_{\text{dust}} < 0.05 M_{\odot}/\text{pc}^2$, where zero level offsets between H I and FIR dominate. Assumptions made are indicated in the corresponding panels.

(sensitivity limit). This spatial correlation is expected from the physics of CO formation and dissociation. The H I envelope of the clouds is more extended than the CO regions, but is also well spatially correlated with the dust surface density. Figure 3 shows the pixel-to-pixel correlation between the dust surface density, the H I surface density, $\Sigma(\text{H I})$, the H₂ surface density derived from CO observations, $\Sigma(\text{H}_2^{\text{CO}})$, and the total gas surface density, $\Sigma_{\text{gas}}^{\text{obs}}$. $\Sigma(\text{H I})$ dominates the gas surface density and increases linearly with Σ_{dust} for $\Sigma_{\text{dust}} < 0.1 M_{\odot}/\text{pc}^2$ ($A_V = 1$), at which point the gas surface density becomes dominated by H₂. The total gas surface density is linearly correlated with the dust surface density over the entire range of dust surface densities. The slope of the correlation gives the gas-to-dust ratio, the value of which is $\text{GDR} = 351 \pm 5$ for NT80, and $\text{GDR} = 234 \pm 4$ for NT71. The intercept of the total gas surface density with the zero dust surface density is at $\Sigma_{\text{gas}}^{\text{obs}} = 1.4 \pm 0.56 M_{\odot}/\text{pc}^2$ for NT80 and $3.8 \pm 0.5 M_{\odot}/\text{pc}^2$ for NT71, indicating that there is an offset between the zero levels of the dust and H I surface density maps. As a result, we do not trust ratios of dust and gas surface densities at low surface densities ($\Sigma_{\text{dust}} < 0.05 M_{\odot}/\text{pc}^2$).

We examine the correlation between two different estimates of the gas surface density: from dust measurements and a constant gas-to-dust ratio, $\Sigma_{\text{gas}}^{\text{dust}} = \text{GDR} \times \Sigma_{\text{dust}}$, and from CO and H I observations, $\Sigma_{\text{gas}}^{\text{obs}}$. The middle panels of Figs. 1 and 2 show the ratio $\Sigma_{\text{gas}}^{\text{dust}} / \Sigma_{\text{gas}}^{\text{obs}}$. On average, the ratio $\Sigma_{\text{gas}}^{\text{dust}} / \Sigma_{\text{gas}}^{\text{obs}}$ is one, with some deviations that appear spatially correlated with the different phases of the ISM. In particular, $\Sigma_{\text{gas}}^{\text{dust}} / \Sigma_{\text{gas}}^{\text{obs}}$ is highest (> 1.5)

in regions with intermediate dust ($\Sigma_{\text{dust}} = 0.1\text{--}0.2 M_{\odot}/\text{pc}^2$) and H I ($\Sigma(\text{H I}) = 20\text{--}30 M_{\odot}/\text{pc}^2$) surface densities, and little or no CO ($\Sigma(\text{H}_2^{\text{CO}}) < 10 M_{\odot}/\text{pc}^2$). It is close to one (> 0.7 and < 1.3) at high dust surface densities ($\Sigma_{\text{dust}} > 0.2 M_{\odot}/\text{pc}^2$ or $A_V > 2$), inside the CO boundary ($\Sigma(\text{H}_2^{\text{CO}}) > 10 M_{\odot}/\text{pc}^2$). It is low (< 0.5) in diffuse regions, outside of the H I and CO contours in Figs. 1 and 2. A low $\Sigma_{\text{gas}}^{\text{dust}} / \Sigma_{\text{gas}}^{\text{obs}}$ ratio at low dust surface densities is uncertain as it is likely dominated by small offsets between the H I and the dust surface density zero levels. On the other hand, the excess of FIR emission (i.e., of dust surface density) in regions with intermediate dust surface density and little or no CO supports the presence of H₂ envelopes not traced by CO, and is consistent with previous conclusions drawn from the comparison between dust and gas (Israel 1997; Leroy et al. 2007, 2009).

Last, the right panels of Figs. 1 and 2 show that the dust temperature appears to be spatially anti-correlated with the dust surface density, the high dust surface density regions being colder than the low dust surface density regions by a few K. This effect is further seen in Fig. 4, which shows the pixel-to-pixel correlation between Σ_{dust} and T_{dust} . This anti-correlation suggests that the regions of MCs that are well shielded from the ambient radiation are colder than the envelopes of the clouds, more exposed to the ISRF. This effect has not been observed at 4' resolution in the dust properties derived from IRAC, MIPS, and IRIS observations of NT80 and NT71 (Paradis et al. 2010), but is clearly seen at 1' resolution in our *Herschel* data. The dust temperature in NT71 is higher than in NT80, which may result from heating by star forming regions embedded in NT71.

4. Possible causes of the variations of $\Sigma_{\text{dust}} / \Sigma_{\text{gas}}^{\text{obs}}$

4.1. X factor variations

The molecular gas surface density derived from CO observations was computed with a constant X factor. In reality, the CO/H₂ abundance is sensitive to photo-dissociation at $A_V < 2\text{--}3$ (Rubio et al. 1993; Glover & Mac Low 2010). As a result, the X factor is expected to decrease (the CO/H₂ abundance to increase) with dust surface density in the transition region between the H₂ envelopes and the CO cores of MCs. While H₂ gas not traced by CO in the envelopes of MCs might account for the excess of FIR emission with respect to the gas surface density *outside* the CO boundary, unaccounted for X factor variations may also cause deviations in the dust/gas correlation *inside* the CO boundary.

Within the CO boundary (where I_{CO} is above the MAGMA sensitivity), we derive the X factor required to match the gas surface density inferred from dust and a constant GDR with the surface density implied by CO and H I observations:

$$X_{\text{CO}}^{\text{obs}} = (\text{GDR} \times \Sigma_{\text{dust}} - \Sigma(\text{H I})) / (2.16 \times 10^{-20} I_{\text{CO}}) \quad (1)$$

The top row of Fig. 5 shows the correlation between $X_{\text{CO}}^{\text{obs}}$ and Σ_{dust} . The red curve indicates the binned trend (0.02 M_{\odot}/pc^2 bins). Since i) we assume a constant X factor, $X_{\text{CO}} = 5.1 \times 10^{20}$ for NT80 and $X_{\text{CO}} = 4.1 \times 10^{20}$ for NT71, to derive GDR, and ii) we assume GDR to derive $X_{\text{CO}}^{\text{obs}}$ at each pixel, it follows that the average of $X_{\text{CO}}^{\text{obs}}$ and the assumed X_{CO} must be and are equal within the error bars ($\langle X_{\text{CO}}^{\text{obs}} \rangle = (5.7 \pm 0.5) \times 10^{20}$ and $(3.6 \pm 0.5) \times 10^{20}$ for NT80 and NT71). Thus, Fig. 5 merely investigates whether systematic variations in $X_{\text{CO}}^{\text{obs}}$ with Σ_{dust} can explain the variations in Figs. 1, 2 and the scatter in Fig. 3.

X_{CO} is higher in the range $\Sigma_{\text{dust}} = 0.1\text{--}0.2 M_{\odot}/\text{pc}^2$ ($A_V = 1\text{--}2$) by a factor of up to 8 compared to the densest regions, well

inside the CO boundary ($\Sigma_{\text{dust}} > 0.2 \text{ M}_{\odot}/\text{pc}^2$ or $A_V > 2$). This enhancement however only appears marginally significant in the binned trends. Nonetheless, X factor variations may very well contribute to the observed variations in the FIR emission/gas surface density ratio inside the CO boundary. In fact, this increase in X_{CO} at intermediate surface densities is likely coincident with the transition regions between dissociated and shielded CO, and supports the presence of H_2 envelopes not traced by CO. The decrease in X_{CO} at low ($< 0.05 \text{ M}_{\odot}/\text{pc}^2$) dust surface densities is likely due to small offsets between the H I and dust surface density zero levels — the H I level being slightly higher, as shown by the negative values of X_{CO} . Besides being difficult to explain physically, we do not trust its significance.

4.2. Dust emissivity variations

The dust surface density was derived assuming that the emissivity of dust does not depend on environment. An emissivity increase in the FIR of a factor 3 to 4 between the diffuse and dense phases has however been invoked to explain the cold temperatures and the $60 \mu\text{m}$ emission deficit observed in the molecular phase (Stepnik et al. 2003), and is expected from grain coagulation in the dense phase of the ISM (Paradis et al. 2009). In the Milky Way, this argument is supported by recent FIR and sub-mm observations by Paradis et al. (2009).

The dust emissivity per unit mass, $\epsilon_{160}^{\text{obs}}$, was derived from matching the $160 \mu\text{m}$ emission to the surface density implied by CO and H I observations for a constant gas-to-dust ratio:

$$I_{160} = \epsilon_{160}^{\text{obs}} \Sigma_{\text{gas}}^{\text{obs}} B_{160}(T_{\text{dust}}) / \text{GDR} \quad (2)$$

where, I_{160} is the brightness observed at $160 \mu\text{m}$, $B_{160}(T_{\text{dust}})$, is the Planck function at the dust temperature T_{dust} and at $160 \mu\text{m}$, and GDR is a constant gas-to-dust ratio.

The second row of Fig. 5 shows the pixel-to-pixel correlation as well as the binned relation between $\epsilon_{160}^{\text{obs}}/\epsilon_{160}^0$ and Σ_{dust} , where ϵ_{160}^0 is the constant emissivity assumed to derive the dust surface density (Gordon et al. 2010). For both NT80 and NT71, $\epsilon_{160}^{\text{obs}}$ is constant with Σ_{dust} within the scatter. Again, we do not take the lowest, uncertain Σ_{dust} points into account. While it is possible that trends be hidden in the scatter, our data do not seem to support emissivity variations as a major contributor to the variations in the FIR emission/gas surface density correlation. Further investigation with the full extent of the HERITAGE survey will be necessary to draw firmer conclusions.

4.3. Gas-to-dust ratio variations

Our analysis in Sects. 4.1 and 4.2 was based on the assumption of a constant gas-to-dust ratio. It is possible, however, that X_{CO} and the FIR dust emissivity are approximately uniform, and that GDR varies. In this case, the middle panel of Figs. 1 and 2 represents the variations in gas-to-dust ratio implied by gas and dust observations. Gas-to-dust ratio variations could be caused by dust destruction (or change of size) in shocks and intense ISRFs in the LMC, or by grain growth in molecular cores.

The gas-to-dust ratio implied by dust and gas observations was obtained via $\text{GDR}^{\text{obs}} = \Sigma_{\text{gas}}^{\text{obs}}/\Sigma_{\text{dust}}$. The plausibility of gas-to-dust ratio variations as a cause for deviations in the FIR emission/gas correlation was further tested by examining the correlation between GDR^{obs} and Σ_{dust} , shown in the bottom row of Fig. 5. The dashed line indicates the constructed trend obtained for a constant, mean gas surface density. If the lowest, uncertain points in Σ_{dust} are omitted, the gas-to-dust ratio

appears rather constant with Σ_{dust} , within the scatter. Although a more complete investigation is needed to draw strong conclusions, gas-to-dust ratio variations between the diffuse and dense phases of the ISM do not appear to contribute much to deviations in the FIR emission/gas correlation.

5. Conclusion

We have examined the correlation between dust, atomic, and molecular gas using HERITAGE, ATCA H I 21 cm, and MAGMA CO observations of two LMC molecular clouds. The dust temperature appears consistently lower in the dense phase than in diffuse regions. The dust surface density is spatially correlated with the atomic and molecular phases, making *Herschel*'s angular resolution and complete coverage of the IR SED a powerful tracer of molecular gas. We have however observed an excess of FIR emission with respect to the gas surface density implied by CO and H I observations, which occurs at intermediate dust surface densities ($0.1\text{--}0.2 \text{ M}_{\odot}/\text{pc}^2$), outside and close to the CO boundary. This likely indicates that molecular clouds are surrounded by envelopes of H_2 not traced by CO. The presence of unaccounted for H_2 envelopes is further supported by an increase in the X factor at intermediate dust surface densities, corresponding to the transition region between dissociated and shielded CO.

We reviewed two alternative explanations for the FIR excess: variations in dust emissivity and the gas-to-dust ratio between the diffuse and dense phases of the ISM. We derived the dust emissivity and gas-to-dust ratio required to match the observations, and examined their correlations with the dust surface density in order to evaluate the plausibility of each hypothesis. We found that the dust emissivity and gas-to-dust ratio in NT71 and NT80 are constant with Σ_{dust} within the scatter, and conclude that dust emissivity and gas-to-dust ratio variations are therefore unlikely to be responsible for the FIR excess observed near these clouds. Variations in emissivity and gas-to-dust ratio between the dense and diffuse ISM phases cannot be definitively ruled out however, due to uncertainties at low dust surface density that are caused by offsets in the zero levels of the H I and dust maps. In the immediate future, we will conduct a full investigation of all these effects using detailed modeling in combination with the completed HERITAGE survey of both Magellanic Clouds.

Acknowledgements. We acknowledge financial support from the NASA Herschel Science Center (NHSC), JPL contracts #1381522, and #1381650. Part of this research was conducted at the Jet Propulsion Laboratory, California Institute of Technology under contract with the National Aeronautics and Space Administration. We thank the support from the European Space Agency, PACS and SPIRE teams, Herschel Science Center, and NHSC (B. Ali, K. Xu). M.R. is supported by FONDECYT No1080335 and FONDAP No15010003.

References

- Bernard, J., Reach, W. T., Paradis, D., et al. 2008, *AJ*, 136, 919
- Davies, R. D., Elliott, K. H., & Meaburn, J. 1976, *MmRAS*, 81, 89
- Fukui, Y., Kawamura, A., Minamidani, T., et al. 2008, *ApJS*, 178, 56
- Glover, S. C. O. & Mac Low, M. 2010, *MNRAS*, submitted, arXiv:1003.1340
- Gordon, K., Galliano, F., Hony, S., et al. 2010, *A&A*, this volume
- Griffin et al. 2010, *A&A*, this volume
- Hughes, A., Wong, T., Ott, J., et al. 2010, *MNRAS*, accepted
- Israel, F. P. 1997, *A&A*, 328, 471
- Kawamura, A., Mizuno, Y., Minamidani, T., et al. 2009, *ApJS*, 184, 1
- Kim, S., Staveley-Smith, L., Dopita, M. A., et al. 2003, *ApJS*, 148, 473
- Leroy, A., Bolatto, A., Stanimirovic, S., et al. 2007, *ApJ*, 658, 1027
- Leroy, A. K., Bolatto, A., Bot, C., et al. 2009, *ApJ*, 702, 352
- Meixner, M., Galliano, F., Hony, S., et al. 2010, *A&A*, this volume
- Meixner, M., Gordon, K. D., Indebetouw, R., et al. 2006, *AJ*, 132, 2268

Pagel, B. E. J. 2003, in *Astronomical Society of the Pacific Conference Series*, ed. C. Charbonnel, D. Schaerer, & G. Meynet, Vol. 304, 187–+
 Paradis, D., Bernard, J., & Mény, C. 2009, *A&A*, 506, 745
 Paradis, D., Reach, W., Bernard, J.-P., et al. 2010, *AJ*, submitted
 Rubio, M., Lequeux, J., & Boulanger, F. 1993, *A&A*, 271, 9
 Schaefer, B. E. 2008, *AJ*, 135, 112
 Stepnik, B., Abergel, A., Bernard, J., et al. 2003, *A&A*, 398, 551
 Szewczyk, O., Pietrzyński, G., Gieren, W., et al. 2009, *AJ*, 138, 1661
 Wolfire, M., Hollenbach, D., & McKee, C. 2010, *ApJ*, submitted

¹ Space Telescope Science Institute, 3700 San Martin Drive, Baltimore, MD 21218, USA e-mail: duval@stsci.edu

² Sterrewacht Leiden, Leiden University, P.O. 9513, NL-2300 RA Leiden, Netherlands e-mail: israel@strw.leidenuniv.nl

³ University of Maryland, Department of Astronomy, Lab for Millimeter Wave Astronomy, College Park, MD 20742, USA e-mail: bolatto@astro.umd.edu

⁴ Centre for Supercomputing and Astrophysics, Swinburne University of Technology, Hawthorn VIC 3122, Australia e-mail: ahughes@astro.swin.edu.au

⁵ CSIRO Australia Telescope National Facility, PO Box 76, Epping NSW 1710, Australia

⁶ National Radio Astronomy Observatory, 20 Edgemont Road Charlottesville, VA 22903-2475, USA e-mail: aleroy@nrao.edu

⁷ CEA, Laboratoire AIM, Irfu/SAP, Orme des Merisiers, F-91191 Gif-sur-Yvette, France e-mail: smadden@cea.fr, sacha.hony@cea.fr, marc.sauvage@cea.fr, Koryo.OKUMURA@cea.fr, pasquale.panuzzo@cea.fr

⁸ Spitzer Science Center, California Institute of Technology, MS 220-6, Pasadena, CA 91125, USA e-mail: paradis@ipac.caltech.edu, reach@ipac.caltech.edu

⁹ Department of Astrophysics, Nagoya University, Nagoya 464-8602, Japan e-mail: kawamura@phys.nagoya-u.ac.jp

¹⁰ University of Missouri, Department of Physics and Astronomy, 314 Physics Building, Columbia, MO 65211, USA e-mail: lia@missouri.edu

¹¹ University of Illinois, Dept. of Astronomy, MC 221, Urbana, IL 61801, USA e-mail: wongt@astro.illinois.edu

¹² Centre d' Étude Spatiale des Rayonnements, CNRS, 9 av. du Colonel Roche, BP 4346, 31028 Toulouse, France e-mail: Jean-Philippe.Bernard@cesr.fr

¹³ Steward Observatory, University of Arizona, 933 North Cherry Ave., Tucson, AZ 85721, USA e-mail: cengelbracht@as.arizona.edu, kmisselt@as.arizona.edu

¹⁴ Sejong University, Astronomy & Space Science, 143-747, Seoul, South Korea e-mail: sek@sejong.ac.kr

¹⁵ National Radio Astronomy Observatory, P.O. Box O, 1003 Lopezville Road, Socorro, NM 87801-0387, USA e-mail: jott@nrao.edu

¹⁶ Jet Propulsion Laboratory M/S 169-507, 4800 Oak Grove Dr., Pasadena, CA 91109, USA e-mail: Jorge.Pineda@jpl.nasa.gov

¹⁷ Stratospheric Observatory for Infrared Astronomy, Universities Space Research Association, Mail Stop 211-3, Moffett Field, CA 94035

¹⁸ Departamento de Astronomia, Universidad de Chile, Casilla 36-D, Santiago, Chile e-mail: rubio.monik@gmail.com